

Research article

Engineering highly aligned continuous nanofibers via electrospinning: A comprehensive study on collector design, electrode geometry, and collector speed

Mehmet Selim Demirtaş^{1*}, Mrinal C. Saha²

¹Mechanical Engineering Department, Hitit University, 19030 Corum, Turkey

²School of Aerospace and Mechanical Engineering, University of Oklahoma 865 Asp Avenue, Norman, 73019 Oklahoma, USA

Received 23 April 2024; accepted in revised form 31 May 2024

Abstract. Nanomaterials, particularly nanofibers produced through electrospinning, have garnered significant attention due to their unique properties and diverse applications. This research explores the influence of collector design, electrode geometry, and collector speed on the properties of electrospun polyacrylonitrile (PAN) nanofibers. Finite element analysis (FEA) was employed to simulate electric fields, revealing the impact of collector geometry on field intensity. The experimental setup, enclosed in an isolated chamber, employed various collector types and electrode configurations. Scanning electron microscope (SEM) analysis showcased the effect of collector speed on fiber alignment and diameter. Furthermore, FEA simulations elucidated the role of electrode geometry and voltage in shaping the electric field, impacting fiber properties. The study introduces a novel, in-house method for producing highly aligned nanofibers and provides insights into optimizing electrospinning parameters for enhanced fiber properties. A testing protocol is devised to minimize surface damage when conducting mechanical tests on nanofiber films, employing a dynamic mechanical analyzer (DMA). Mechanical testing demonstrated the correlation between alignment and tensile strength. Overall, this research contributes valuable insights for tailoring electrospinning processes for tissue engineering and energy storage.

Keywords: electrospinning, nanofibers, polyacrylonitrile (PAN), FEA, tensile testing

1. Introduction

The benefits of nanomaterials have ushered in significant changes in today's technology. Furthermore, the growing demand for nanotechnology serves as a strong motivation for scientific research in this field. The reduction in size to the nanoscale is the foundation of numerous advantages, including a high surface area, elevated surface energy, and favorable mechanical properties. Among many other nanotechnology materials, nanofibers have a high potential in various applications such as reinforcements [1–3], fillers [4–7], supercapacitors [8–11], batteries [5, 8, 12–18], filters [10, 11, 19–22], electrochemical

sensors [23–28] and biomaterial [29–37]. The electrospinning method has been identified as one of the most effective approaches for producing continuous nanofibers. It involves using a polymer solution comprising a solvent and a polymer [38].

Conventional spinning methods such as dry spinning, melt spinning, and wet spinning utilize mechanical forces to reduce fiber diameter to a few micrometers. In contrast, the electrospinning method harnesses a high electrical potential difference to generate a mechanical force that reduces fiber diameter to the nanoscale [39, 40]. The formation of a Taylor cone is a crucial stage in the electrospinning

*Corresponding author, e-mail: mehmetseimdemirtas@hitit.edu.tr
© BME-PT

process. When a liquid polymer solution or melt is exposed to an electric field above a certain threshold voltage, the liquid droplet at the needle tip stretches into a characteristic cone shape called the Taylor cone. From the tip of this cone, a fine jet of charged particles, typically polymer fibers, is emitted [40]. The jet's trajectory and stability are vital for producing uniform and continuous fibers. Researchers examine various aspects of the jet, such as its diameter [41], movement [42], and solidification [43]. Understanding the dynamics of the Taylor cone and the electrospun jet is essential for optimizing the process and customizing nanofiber properties.

The molecular weight of a polymer significantly influences the electrospinning process. High-molecular-weight polymers are preferred because they provide better chain entanglement, leading to continuous and uniform nanofiber formation. Longer polymer chains enhance mechanical stability and prevent premature jet rupture [44]. Additionally, the solution properties, such as viscosity, surface tension, and conductivity, are affected by molecular weight. Extremely low molecular weight solutions tend to form beads instead of fibers, while high molecular weight solutions yield larger-diameter fibers [45]. An increase in molecular weight and solution concentration enhances the tensile strength and modulus of the fiber mat. Ngadiman *et al.* [46] claimed that the improvement in mechanical properties decreases once the molecular weight exceeds 145 kDa.

Alharbi *et al.* [47] examined the mechanical properties of nanofibers electrospun from polycaprolactone (PCL) with molecular weights of 74, 114, and 150 kDa. The results indicated that molecular weight had only a minor impact on the mechanical properties of the fibers. Nanofibers from all three molecular weights exhibited similar tensile properties.

The fabrication process can yield either random non-woven structures or consistently aligned yarns, and this outcome depends on various process parameters and the type of collector used [48, 49]. Aligned polymer fibers possess the capability to control cell migration, proliferation, and differentiation, which is vital in the context of tissue engineering. Moreover, highly aligned fibers have shown enhanced performance in fuel cell applications [48]. Aligned nanofibers are essential for enhancing cell migration [50], differentiation [51], and tissue regeneration [52]. They replicate the natural alignment of nerve fibers and utilize their inherent electric fields to foster an

environment that supports cell activities beneficial for tissue repair and healing. For instance, in peripheral nerve regeneration, nerve guidance conduits (NGCs) composed of aligned electrospun nanofibers attract macrophages. This process subsequently aids the migration and myelination of Schwann cells, significantly contributing to peripheral nerve regeneration in animal studies [52, 53].

The production of aligned nanofibers through electrospinning typically involves the use of purpose-built fiber collectors, including a high-speed rotating disc collector [49, 54] or a parallel electrode collector [55]. In a parallel-electrode setup, the insulating space between two parallel electrodes serves as the fiber collector. Charged fibers are aligned across this gap due to the electric field generated near the edges of the electrodes, which directs the fibers perpendicular to the electrode edges. The length of the aligned fibers is constrained by the width of the insulating gap in a configuration with a rotating collector.

In this setup, the polymer fibers are generated and then placed onto a rotating mandrel. Alternatively, in the case of a rotating collector type, the polymer fibers are deposited onto and wound around a rotating disc. The extent of fiber alignment and the diameter of the fibers are primarily influenced by the rotational speed of the mandrel. Kiselev and Rosell-Llompart [55] conducted research showing that an increase in the speed of the collector wheel led to a decrease in fiber diameter and an enhancement in the degree of alignment. Furthermore, Haider *et al.* [56] successfully reduced the fiber diameter from 163.9 to 137.4 nm by elevating the collector surface speed from 2.09 to 21.98 m/s.

Manipulating the electric field is another method for fabricating aligned nanofibers. Ramya and Sangaranarayanan [26] employed two parallel auxiliary electrodes to minimize lateral motion. Sharma and Chung [27] improved fiber alignment by applying a secondary electric field perpendicular to the fluid jet. Ünsal and Bedeloğlu [28] modified the parallel electrode method by adding a positively charged ring to the collector alongside parallel electrodes. They reported that the additional ring enhances fiber alignment.

The design of electrodes or needle tips plays a significant role in shaping the electric field, and collector geometry also affects the process. Needles are frequently used to direct the solvent, which later forms into droplets. Using a needle has several benefits,

including simplicity, ease of upkeep, and prevention of orifice blockages. Nonetheless, this technique demands a relatively high voltage. In contrast, spinneret systems are utilized to achieve consistent fiber diameters with a lower voltage requirement [29]. Spinneret configurations without the need for needles are known as “needleless” systems. They encompass different designs, including flat spinnerets [30–32], rotating wire spinnerets [33], metal roller spinnerets [34], and stepped pyramid spinnerets [35]. Needleless electrodes can be designed with multiple openings, leading to higher production rates. Typically, these systems are employed for large-scale production of fiber mats and utilize relatively larger collectors, such as cylinders [29]. Nonetheless, it is worth noting that a flat-type spinneret electrode yields more consistent electric fields [30, 31].

While using additional electrodes to manipulate the electric field can enhance fiber alignment, it necessitates the incorporation of complex supplementary components. In this research, a straightforward, in-house method has been devised to produce exceptionally aligned continuous nanofibers. Various collector designs, electrode configurations, and collector velocities have been improved to achieve the production of highly aligned electrospun nanofibers. Our study focuses on manufacturing highly aligned nanofibers and examining how the properties of electrospun PAN nanofibers, produced from a solution of 10% polyacrylonitrile (PAN) in *N,N*-dimethylformamide (DMF), are influenced by variations in collector design, electrode geometry, and collector speed. Since electric field distribution influences fiber diameter and the finite element method (FEM) is widely used to investigate electric field characteristics [57–59], an open-source 2D finite FEM software FEMM 4.2 was utilized to analyze the electric field distribution as a function of collector and electrode geometry. Additionally, the characteristics of Taylor cone and jet have been studied by employing a high-speed camera to understand the effects of electric field distribution on jet formation. The alignment of the nanofibers produced during the electrospinning process was altered by changing the collector’s geometry, which included copper foil, mesh, and wire, as well as adjusting the collector speed within the range of 9.9 to 29.8 m/s, while keeping all other electrospinning parameters constant. We examined the diameter distribution and alignment of the fibers using a scanning electron

microscope (SEM). Tensile tests have been performed using a dynamic mechanical analyzer (DMA) to measure changes in mechanical properties depending on the collector and electrode design.

2. Methods

2.1. Electric field analysis

Analyzing electric field distribution and strength is crucial for manipulating fiber orientation and ensuring fiber quality. The study employed finite element analysis, with the open-source software FEMM 4.2 (Waltham, MA, USA) to simulate electric fields across various collector geometries. Experimental setup conditions were applied as boundary conditions, assuming full insulation of the electrospinning setup box. The distance between the needle and collector was set at 18 cm. The needle carried a positive charge of 15 kV, while the collector was simulated as grounded (0 V). The relative electric permeability of air, needle tip, and collectors was set to 1, and the impact of relative humidity on air permeability was disregarded due to its negligible effect. Electric field and voltage distribution were examined in 2D for all collector types.

2.2. Experimental

2.2.1. Electrospinning setup

To mitigate the influence of environmental factors such as moisture, temperature, and electrical noise, the electrospinning setup was enclosed in an electrically and environmentally isolated acrylic box. Nevertheless, to ensure control over the relative humidity level, an air inlet was strategically positioned on the box wall. This inlet facilitates the introduction of either dry or humid air, allowing for the maintenance of a consistent relative humidity level within the setup.

Figure 1 shows the schematic overview of the configuration. The collector wheel was affixed to a shaft, supported at both ends by ball bearings, and the core shaft, crafted from an aluminum tube, maintained concentricity at high speeds. A polyvinyl chloride (PVC) pipe was utilized to insulate the shaft. Additionally, two detachable disks, bolstered by ribs, were utilized to modify the collector width. Vibration was minimized through the implementation of a belt drive speed control motor system. To ensure a constant relative humidity level during electrospinning, an air control unit was incorporated into the setup.

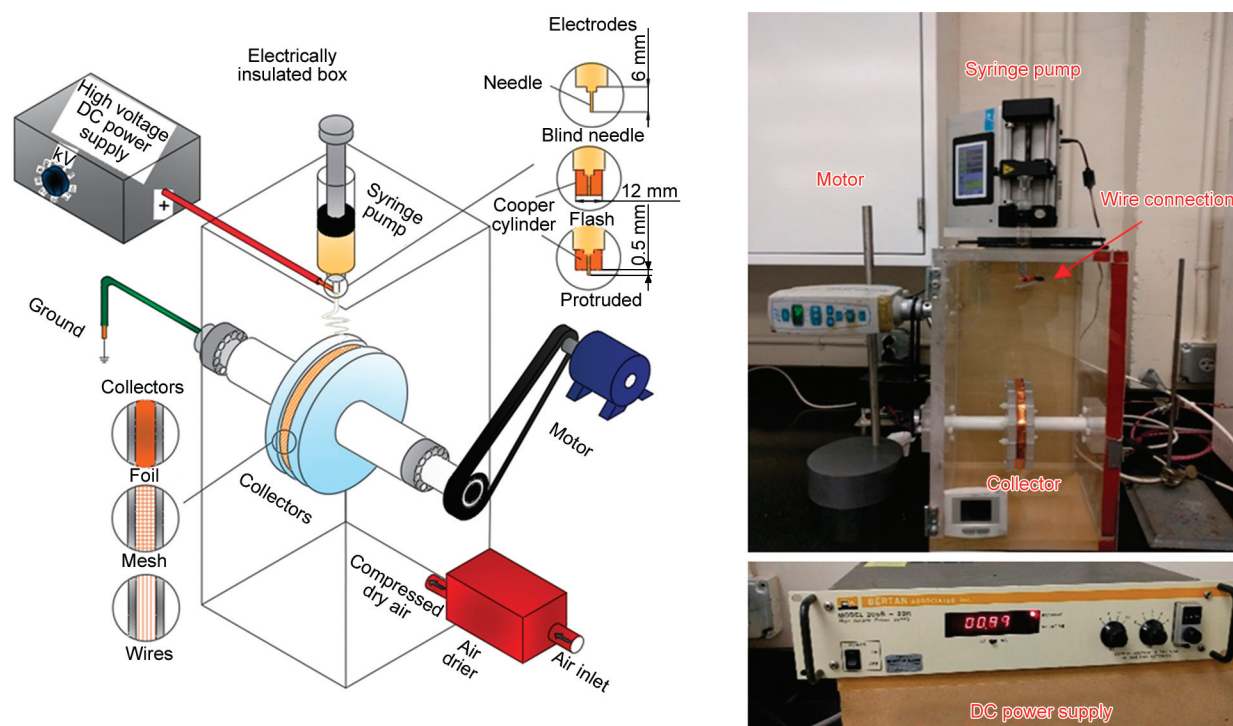


Figure 1. Schematic (left) and actual (right) view of the electrospinning setup.

2.2.2. Electrospinning

N,N-dimethylformamide (DMF) $\geq 99.8\%$ (Sigma-Aldrich, Missouri, USA) solvent and Polyacrylonitrile (PAN) with an average molecular weight of approximately 150 000 g/mol were sourced from Sigma-Aldrich (Missouri, USA). The PAN underwent a 24 h drying process in a vacuum oven to eliminate any remaining moisture. A solution containing 10% PAN in DMF (by weight) was prepared using a magnetic stirrer and a hot plate set at a constant temperature of 80 °C and a stirring speed of 400 rpm for a continuous duration of 5 h. Prior to electrospinning, all air bubbles were thoroughly removed from the solution. The electrospinning process took place within a closed chamber designed for electrical isolation. The spinning solution was housed in a vertical syringe (53100L Single Syringe Pump, KD Scientific Legato, Holliston, MA, US) featuring a stainless-steel needle connected to a DC power supply Bertan Associates 205B-03R, Hicksville, NY, US.

Figure 1 illustrates three distinct collector types, with copper chosen for its conductivity. The collectors were fashioned as follows: a 0.1 mm thick and 12 mm wide foil, a copper mesh with a wire diameter of 0.3 mm and an opening size of 1.3 mm, and a copper wire with a diameter of 0.3 mm. These collectors were affixed to a 20 cm plastic disc using glue and soldered to a ground wire. The needle was consistently positioned 18 cm above the disk surface.

In a prior study, the optimal flow rate was determined, ensuring a continuous and stable jet flow with an electrospinning voltage of 15 kV and a flow rate of 15 $\mu\text{l}/\text{min}$ [40]. We applied identical parameters to ensure a stable jet during the electrospinning process, resulting in enhanced mechanical properties of the as-spun fiber yarns. The relative humidity was consistently maintained at 22% by introducing the appropriate mix of moist and dry air into the chamber, and this level was identified as optimal for achieving the highest tensile properties [60]. Electrospinning was conducted at various collector surface speeds: 9.9, 14.8, and 29.8 m/s. The temperature was held constant at 20 °C. Once the desired amount of solution (50 μl) was deposited, the collectors were removed from the disc.

Additionally, we investigated three different electrode configurations along with the traditional needle tip. Figure 1 provides a schematic view and dimensions of the electrodes: stainless needle (inner diameter: 0.41 mm, outer diameter: 0.80 mm), flash (outer diameter: 12 mm, inner diameter: 0.8 mm, thickness: 6 mm), and protruded (outer diameter: 12 mm, inner diameter: 0.8 mm, thickness: 5.5 mm). In the flash needle configuration, the stainless-steel needle is positioned inside a copper cylinder, while the protruded needle configuration involves placing the stainless-steel needle in a copper cylinder with the needle protruding 0.5 mm beyond the copper

cylinder. The formation of Taylor cone and the geometry of the straight jet were examined using a high-speed optical camera.

2.2.3. Characterization

SEM images were utilized to explore fiber orientation and diameter distribution. The deposited nanofibers were affixed to the SEM sample holder using collectors, followed by sputter coating with iridium. The examination was conducted using a Tescan VegaII SEM (Brno – Kohoutovice, Czech Republic). Mechanical testing was carried out using a TA Instruments DMA Q800 (New Castle, DE, USA). Preserving fiber alignment was crucial for the investigation. A method has been developed to measure tensile properties with high accuracy.

Figure 2 illustrates the procedure for preparing mechanical test samples. A stainless steel punch system was devised to uniformly cut all cardboard window frames, enabling the mounting of fibers along the deposition direction. To minimize damage during

handling and mounting, samples were affixed to a paper window frame using double-sided tape. The gauge length was set at 6 mm, and the strain rate was maintained at 0.001 s^{-1} . The cross-sectional area of the as-spun nanofiber yarn sample was determined by dividing the yarn's mass by the sample length and the density of PAN polymer, with the PAN density assumed to be 1.18 g/cm^3 [61]. The cross-sectional area was derived through volume calculations. The mean diameter, obtained through SEM fiber diameter analysis, was used to determine the total number of fibers in the as-spun yarn (Equation (1)):

$$A_a = N \frac{\pi d_{am}^2}{4} \quad (1)$$

where N is the number of fibers in the yarn, d_{am} is the mean diameter of as-spun nanofibers, A_a is the total cross section area of as-spun yarn.

A Nikon D5200 digital optical camera is utilized to capture images of the Taylor cone. For high-speed recording, a Redlake Motion Pro X3 camera with a

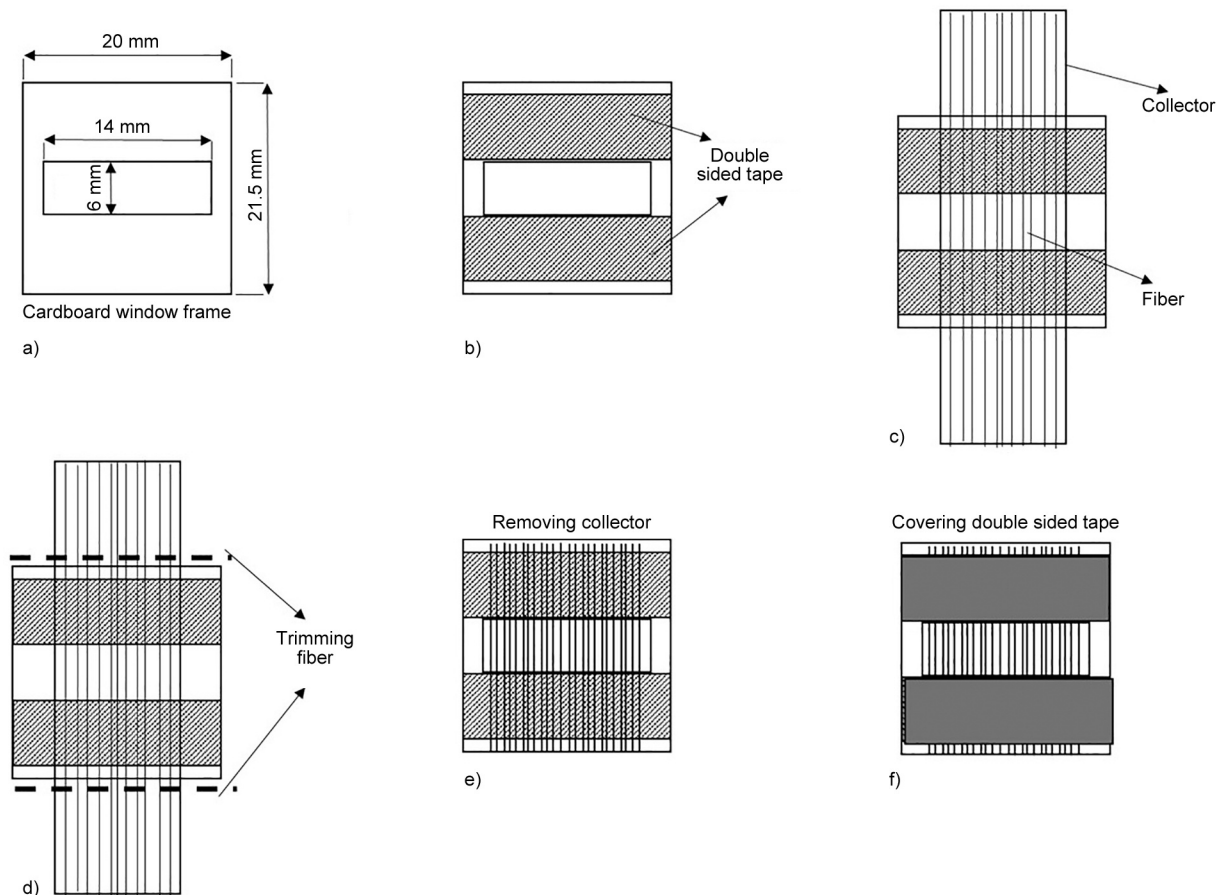


Figure 2. a) Cutting cartoon board window frame via the mold. b) Placing double-sided tape on both ends of the frame. c) Sticking fibers on tape by gently pressing foil. d) Trimming yarn from the top and bottom sides of the window frame. e) Removing collector. f) Closing the other side of the double-sided tape with cartoon slides so that it will not stick to the test fixture.

25 mm manual lens is employed, and the setup is illuminated by a 1000 W halogen light source. The high-speed camera captures images at a rate of 1000 frames per second [fps] with a 100 μ s exposure time. Optical camera images are then analyzed to assess the Taylor cone angle, Taylor cone area, and jet type. The flow is monitored for around 5 min, and intermittent images are captured. ImageJ is used to determine the angle and area of the Taylor cone. For each control group, 100 images are captured using the high-speed camera. ImageJ is then utilized to extract information on the straight jet length, diameter, and

angle. Fiber diameter distribution and orientation analyses are conducted using the ImageJ software. Four SEM images are taken for each sample, and individual fiber diameter and orientation angles are obtained from a total of 100 fibers.

3. Results and discussion

The FEM analysis in Figure 3 displays the outcomes of simulations involving foil, mesh, and wire collectors, exhibiting only half of the simulation due to symmetry. The results highlight the influence of collector geometry on the intensity and distribution

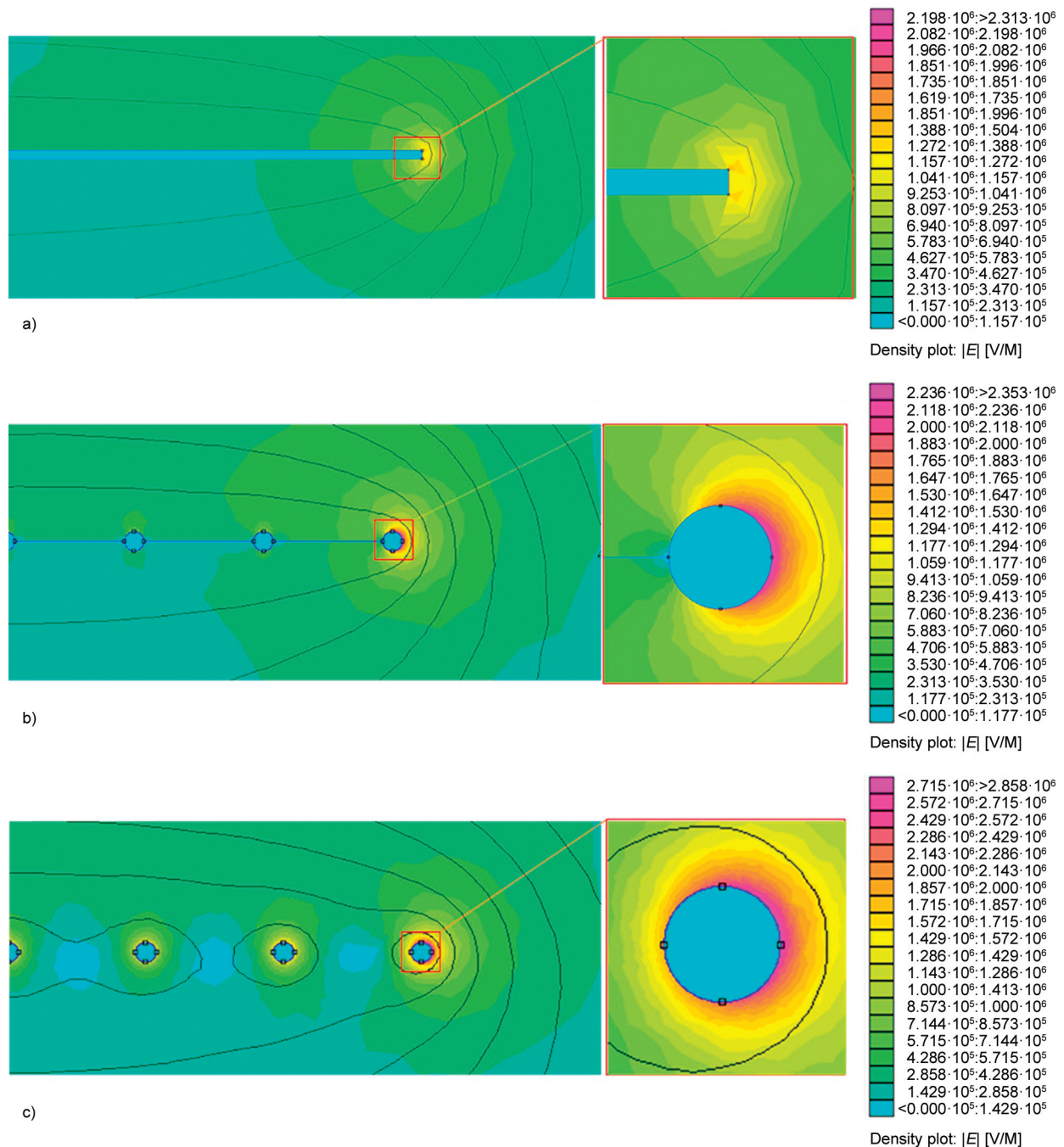


Figure 3. Electric field density distribution of foil (a), mesh (b) and wire (c) type of collector.

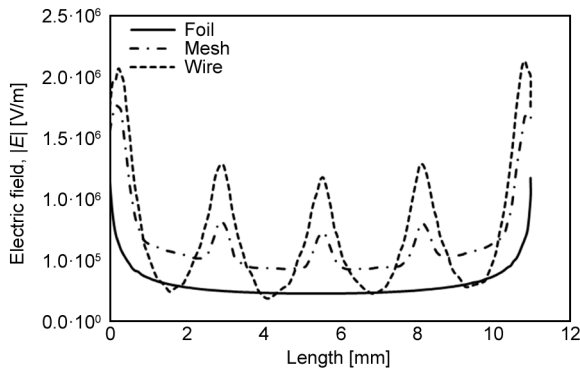


Figure 4. Variation of the electric field along the width of the collector surface for foil, mesh and wire type of collector.

of the electric field. Notably, the foil collector demonstrated higher electric field intensity near its corners, whereas wire and mesh collectors showcased a more uniform and intense electric field overall, surpassing the foil collector in this aspect. Additionally, the electric field intensity was notably higher on the surface of wire and mesh collectors compared to foil collectors.

Figure 4 illustrates the variations in the electric field along the collector for the different collector types. The 2D FEM analysis data reveals that the highest values are found along the sides of the collectors. Interestingly, for wire and mesh collectors, the peaks occur at the center where individual wires are positioned, deviating from the general trend observed in other collector types.

Through FEA, the impact of electrode diameter on electric field distribution is explored. Figure 5 depicts the electric intensity between the electrode and collector, comparing the surface of a 2 mm diameter electrode needle to a 12 mm diameter flash needle. As the electrode diameter increases, a more even electric field distribution becomes evident. Specifically, the needle electrode displays a sudden decrease,

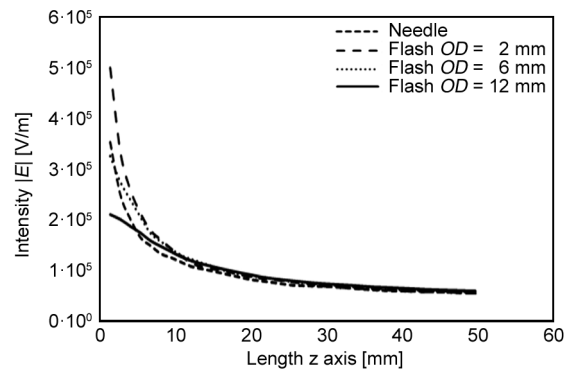


Figure 5. FEA result of electric field intensity from the electrode through the collector, the potential difference is 15 kV for the needle, flash type OD = 2, 6, and 12 mm.

whereas the flash-type electrode exhibits a more gradual reduction in electric field intensity.

Figure 6 exhibits color-coded electric field distribution outcomes for three electrode geometries: needle, flash, and protruded. Both flash and protruded configurations display similar behavior in electric field intensity. A 0.5 mm sputtered needle, when contrasted with a flat surface flash electrode, does not notably alter the electric field. However, the electrode needle demonstrates an exceptionally intense electric field, specifically on its surface.

In Figure 7, a numerical comparison of electric field intensity between the electrode surface and collector (on the z-axis) is presented for all three electrode types. The intensity ranges from $50 \cdot 10^3$ to $20 \cdot 10^4$ V/m along the z-axis. Flash and protruded electrodes exhibit a tendency to maintain higher intensity compared to needle electrodes.

The impact of applied voltage on the electric field is examined through FEA simulations. Figure 8 illustrates the influence of varying applied voltages on electric field intensity along the z-axis for the flash electrode. The analysis covers voltages ranging from

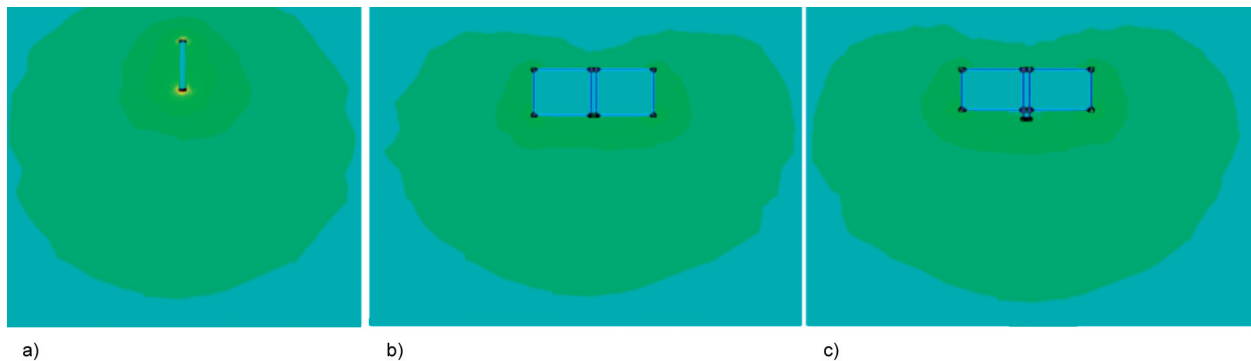


Figure 6. FEA plots of electric field intensity around needle tip where the potential difference is 15 kV for a) needle, b) flash, and c) protruded type of electrode.

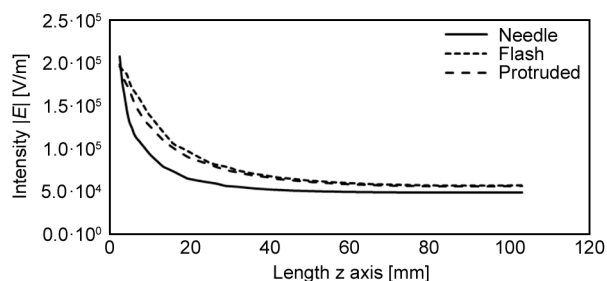


Figure 7. Electric field intensity from electrode through the collector where potential difference is 15 kV for needle, flash, and protruded type of electrode.

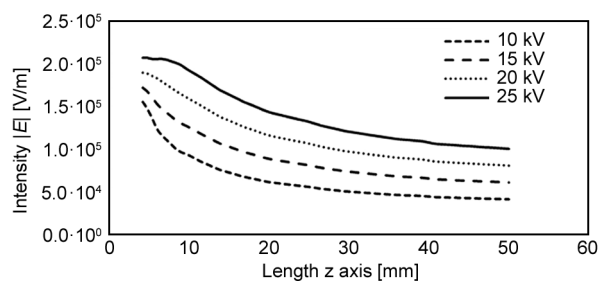


Figure 8. FEA result of electric field intensity as a function of applied voltage from electrode through the collector.

10 to 25 kV. At lower applied voltages, there is a notable trend: The electric field intensity undergoes swift changes along the z-axis compared to higher voltages, specifically at 20 and 25 kV.

In [Figure 9](#), several SEM images of as-spun nanofibers produced under different rpm settings and collector geometries are displayed. These SEM results reveal that, at this low magnification, the nanofibers appear uniform and devoid of defects. Over 100 measurements of various fiber diameters were conducted from SEM images taken at different locations within the nanofiber tows. The angle distribution appears to be more widely spread at 9.9 m/s in comparison to 29.8 m/s. Lower RPM settings resulted in less ordered fibers, which was particularly noticeable with the foil collector. Nonetheless, a noteworthy improvement in the organization of fibers was accomplished by elevating the collector speed, as depicted in [Figure 9a–9c](#). At 1500 rpm, 78% of fibers fall within the 0–5° range, whereas only 34% do so at 500 rpm. In the case of mesh and wire collectors, a higher degree of fiber alignment is achieved, with over 90% of fibers falling within the 0–5° range.

[Figure 10](#) illustrates the standard deviation of angle distributions plotted against rpm. For the foil collector, the standard deviation experiences a sharp decrease between 500 and 1500 rpm. As for wire and mesh collectors, the standard deviation slightly

Table 1. Summary of diameter distribution of as-spun nanofibers at different rpm.

Collector	RPM	As-spun	
		Mean [nm]	Standard deviation [nm]
Foil	500	272	55
	1000	257	51
	1500	245	48
Mesh	500	261	52
	1000	244	42
	1500	241	39
Wire	500	240	51
	1000	242	40
	1500	239	36

diminishes with an increase in collector speed, reaching the most favorable alignment at 1500 rpm for the wire collector type.

[Table 1](#) presents the average fiber diameter and standard deviation for all as-spun nanofibers at various RPM settings. To determine the average fiber diameter, 100 measurements of individual fiber diameters were taken from SEM images captured at various locations within the nanofiber tows. There is a noticeable decrease in the average fiber diameter when the collector speed is increased. Wire and mesh-type collectors exhibit slight enhancements beyond 1000 rpm. This reduction can be attributed to incoming fibers in the air undergoing additional mechanical stretching as they connect to the initially deposited fibers. Consequently, this phenomenon results in a higher degree of alignment.

FEA simulations align with the diameter and angle analyses derived from SEM images. The distribution of the electric field notably influences fiber orientation, with individual wires exhibiting a relatively intense electric field compared to a foil collector. Fiber filaments tend to accumulate in regions where the electrical force is stronger. The geometry of wire and mesh collectors contributes to superior fiber alignment owing to the relatively intense electric fields present on individual wire surfaces. Despite the mesh collector sharing similar wire openings and wire diameters, the interconnection between wires diminishes the electric field. Wire collectors reach a maximum electric field intensity of $2.715 \cdot 10^6$ V/m, whereas mesh collectors produce $2.236 \cdot 10^6$ V/m.

[Figure 11](#) presents higher magnification SEM images displaying nanofibers produced using needle ([Figure 11a](#)), flash ([Figure 11b](#)), and protruded electrode types ([Figure 11c](#)). The utilization of flash and

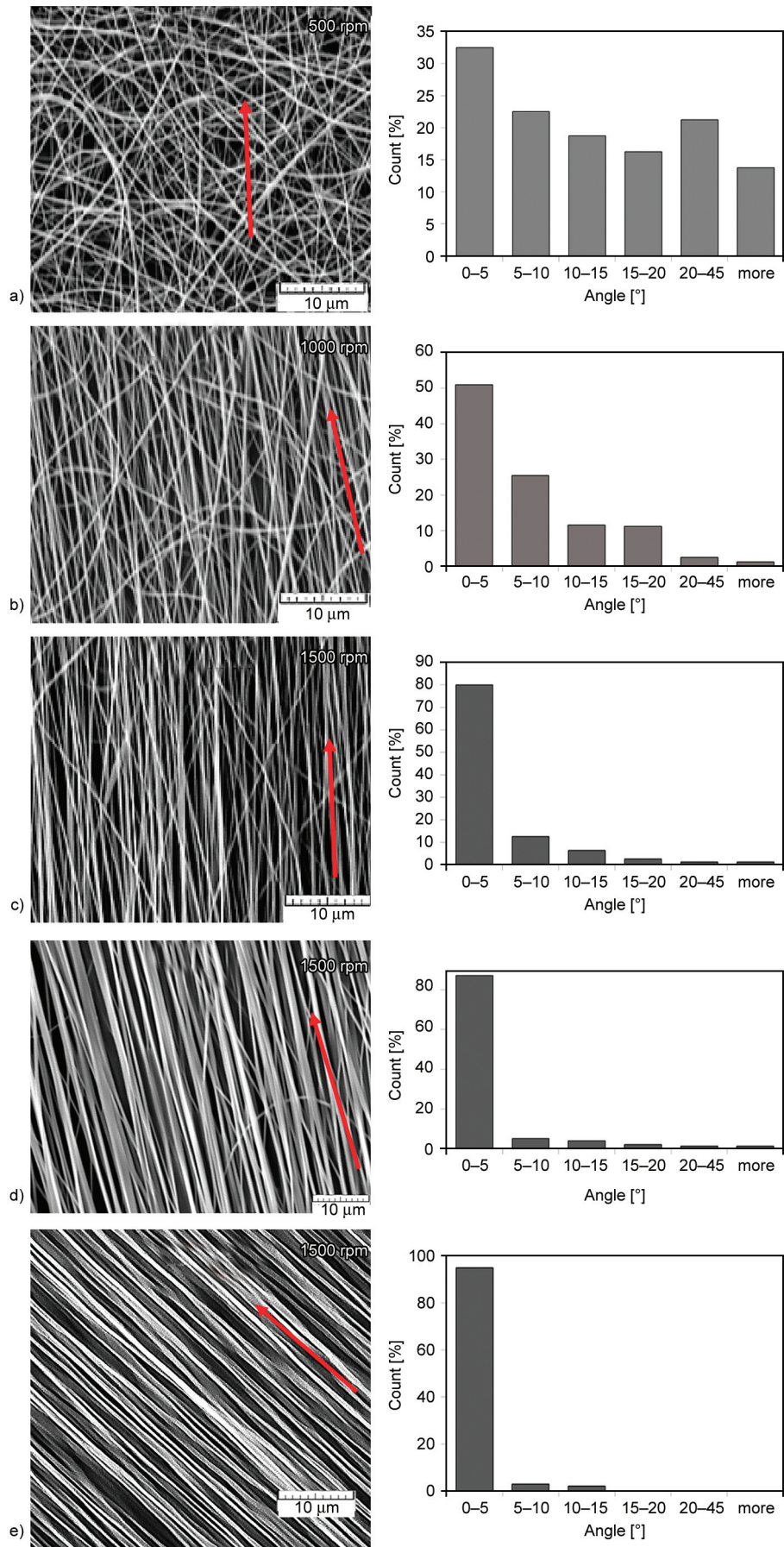


Figure 9. Histograms of PAN nanofiber angle distributions relative to mean orientation, a)–c) copper foil collector, d) metal mesh and e) wire collector. Red arrows indicate the rotation direction of the disc.

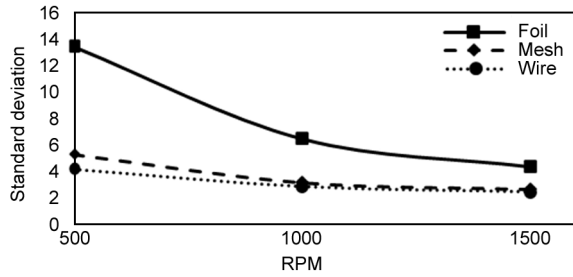


Figure 10. Standard deviation of electrospun PAN angle distributions as the function of collector plate speed.

protruded electrodes results in slightly more uniform and thinner fibers compared to those generated by needle electrodes. [Table 3](#) compiles the average fiber diameter and standard deviation data for electrospun PAN nanofibers across various electrode

types. The diameter of nanofibers undergoes a reduction based on the type of electrode used. Among these, the protruded electrode yields the smallest average diameter and standard deviation.

[Table 2](#) additionally presents data on the diameter of individual fibers and their standard deviation along a single fiber. Fibers produced using flash and protruded electrodes exhibit higher uniformity and smaller diameters. This phenomenon is explained by the FEA outcomes: fibers are exposed to a more uniform electric field along the z-direction when utilizing flash and protruded electrodes. Among these, fibers created with protruded electrodes show slightly smaller diameters and greater uniformity compared to those produced with flash electrodes. The

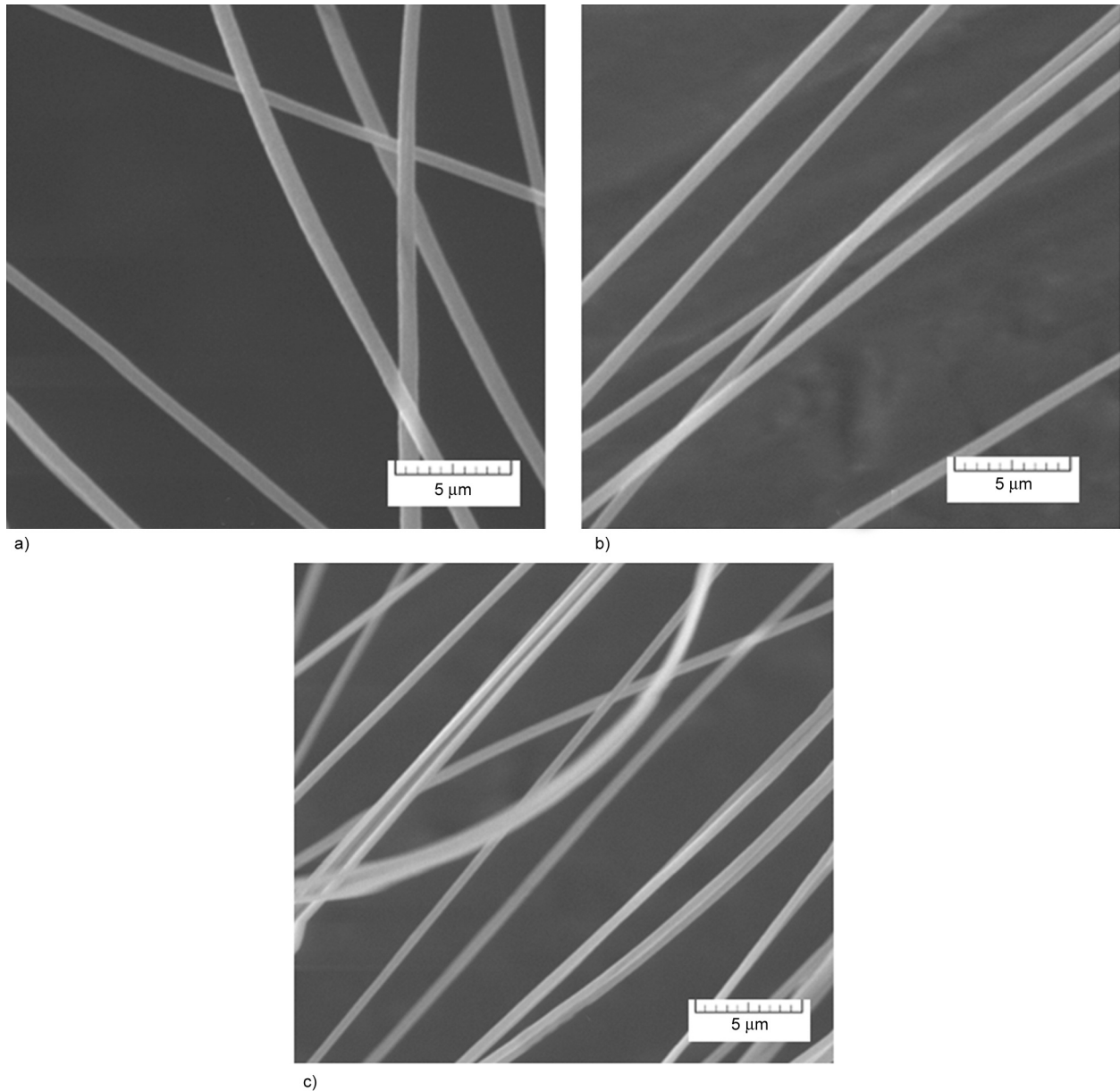


Figure 11. Morphology SEM images of PAN yarn fabricated with a) needle, b) flash, and c) protruded type of electrode.

Table 2. The comparison of diameter distribution on the fiber mat and along a single fiber depends on electrode types.

Geometry		Blind needle	Flash	Protruded
Average fiber diameter of the mat	[nm]	262±50.1	241±38.5	239±35.9
Average fiber diameter along one single fiber	[nm]	258±42.1	243±36.5	241±33.9

Table 3. Summary of optic camera analysis of Taylor cone angle, area and jet type at different flow rates.

Type	Flow rate [μl/min]	Angle [°]	Taylor cone's area [mm ²]	Jet type
Needle	8	50.9	0.106	Narrow intermittent continuous
	10	62.5	0.197	Continuous
	12	64.7	0.432	Continuous
	13	72.9	0.613	Continuous
	15	94.8	0.637	Continuous with intermittent drops
Flash	8	63.1	4.236	Narrow intermittent continuous
	10	67.4	6.256	Narrow intermittent continuous
	12	76.4	8.157	Continuous
	13	77.9	9.006	Continuous
	15	76.6	8.971	Continuous
	20	81.4	9.964	Continuous
	25	105.5	12.550	Continuous with intermittent drops
Protruded	8	55.1	2.979	Narrow intermittent continuous
	10	55.8	3.221	Continuous
	12	63.2	5.021	Continuous
	13	66.2	6.441	Continuous
	15	67.3	6.599	Continuous
	20	98.1	8.231	Continuous with intermittent drops

shape of the electrode also influences the formation of the Taylor cone. The broader flat surface on the flash electrode leads to a wider Taylor cone, impacting fiber formation during electrospinning. Furthermore, the type of electrode can manipulate fiber alignment, with flash and protruded electrodes resulting in superior fiber alignment compared to the needle electrode due to exposure to a less uniform electric field.

This study investigates the variation in Taylor cone shapes influenced by processing conditions and electrode geometries. An optical camera is utilized to

examine Taylor cone formations under different flow rates. Figure 12 displays diverse Taylor cone morphologies observed for various electrode geometries (needle, flash, and protruded) at a flow rate of 13 μl/min and 15 kV. Changes in Taylor cone angle, Taylor cone area, and jet types are monitored across these flow rates. The flash electrode generates a larger Taylor cone with wider angles owing to droplet development on its larger surface area in contrast to the needle tip. Upon the application of voltage to the needle tip, a straight jet formation occurs immediately, whereas, for flash electrodes, a certain solution

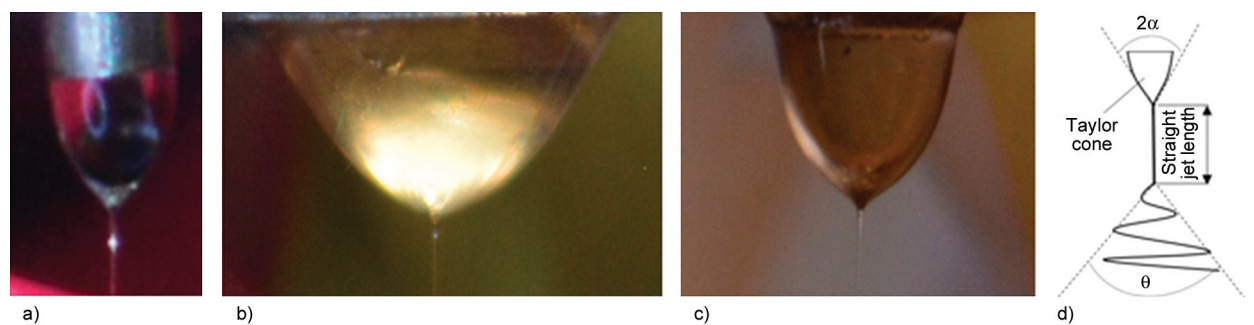


Figure 12. Taylor cone shape at 13 μl/min flow rate and 15 kV for a) needle tip, b) flash, c) protruded, d) demonstration of Taylor cone half angle α , straight jet length, and θ cone angle.

accumulation (between 30 to 40 μl) is necessary to develop the straight jet. Table 3 provides an overview of the Taylor cone angle, area, and jet type across various flow rates. At higher flow rates, there's an occurrence of intermittent droplets due to inadequate charge density, resulting in an inability to remove fluid continuously. When the flow rate is decreased below a critical value, it leads to a narrow intermittent continuous jet regime. The half angle (α), as depicted in Figure 12, increases as the flow rate goes up. For the needle electrode, α ranging between 31.2 and 36.4° corresponds to a continuous flow jet at flow rates of 10 and 13 $\mu\text{l}/\text{min}$, respectively. Yet, the range for continuous jet flow is identified from 12 to 20 $\mu\text{l}/\text{min}$, correlating with α angles of 31.2 and 40.7°, respectively. Specifically, the half angle associated with continuous jet flow falls within the range of 32 to 46° [62]. For protruded electrodes, a consistent jet flow devoid of intermittent drops or interruptions is achieved within the range of 10–15 $\mu\text{l}/\text{min}$, whereas for flash electrodes, this stable flow jet is observed within the range of 12–20 $\mu\text{l}/\text{min}$. Comparatively, there exists a broader range of flow rates ensuring a stable flow jet when using protruded and flash electrodes in contrast to needle electrodes. To explore deeper into the bending mechanisms occurring at the tip of the straight jet, a more robust characterization technique is essential. A high-speed camera is utilized to scrutinize parameters such as straight jet length, diameter, and cone angle (Figure 12d). It's evident that electrode geometry plays a substantial

role in determining the attributes of bending loops and whipping instability. Moreover, the applied voltage directly impacts the characteristics of the straight jet and whipping phenomenon. Under an applied voltage of 15 kV, both flash and protruded electrodes produce longer straight jets compared to the needle electrode, as indicated in Figure 13. Furthermore, flash and protruded electrodes yield thinner straight jet formations in contrast to those formed by the needle electrodes.

Changes in applied voltage lead to modifications in straight jet formation. Likewise, at higher voltages, the formation of straight jets varies depending on the type of electrode used. Notably, an increase in applied voltage corresponds to an increase in straight jet length. Table 4 provides a summary of the analysis from high-speed camera images. Across various electrode types and applied voltages ranging from 15 to 19 kV, a discernible trend emerges. The diameter and length of the straight jet expand with an escalation in positive discharge on the electrode. Moreover, the onset angle for the commencement of the whipping motion is influenced by both electrode type and applied voltage.

FEA simulations indicate that electric field distribution can be controlled by adjusting electrode geometry and changing applied voltage. Flash and protruded electrodes yield a more consistent electric field distribution along the z-axis. When the applied voltage is increased, a more uniform electric field distribution is achieved. Consequently, longer and

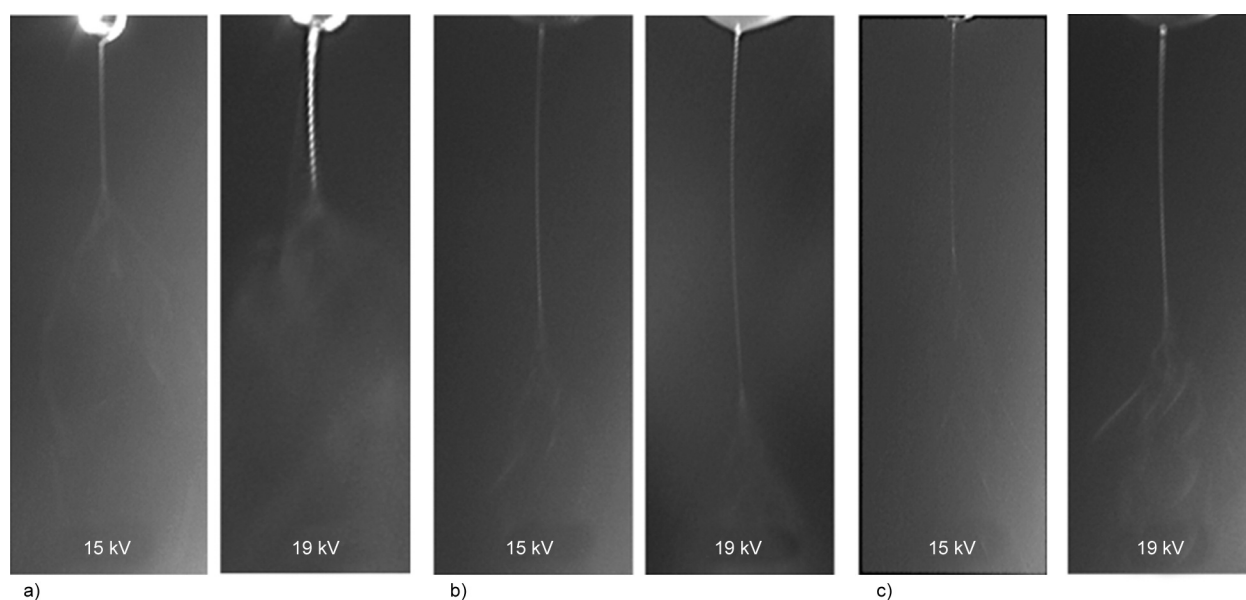


Figure 13. High-speed camera image of the a) needle, b) flash, and c) protruded type of electrode (15 and 19 kV, 13 $\mu\text{l}/\text{min}$ flow rate, 1000 fps, and 100 μs exposure).

Table 4. Summary of high-speed camera image analysis of jet.

Type	Voltage [kV]	Angle [°]	Straight jet length [mm]	Diameter of jet [mm]
Needle	15	67.9	2.82	0.153
	16	62.8	3.01	0.175
	17	50.6	3.41	0.180
	18	47.2	3.77	0.186
	19	43.8	3.95	0.197
Flash	15	56.7	5.80	0.101
	16	50.4	5.99	0.106
	17	49.3	6.04	0.112
	18	45.9	6.47	0.114
	19	39.6	6.83	0.127
Protruded	15	61.3	4.95	0.112
	16	53.1	5.30	0.119
	17	49.7	5.39	0.120
	18	46.7	5.49	0.123
	19	40.1	5.75	0.125

Table 5. Tensile properties of as-spun respected to rpm.

Collector	RPM/surface speed [m/s]	As-spun	
		Tensile strength [MPa]	Tensile modulus [GPa]
Foil	500/9.9	128	5.1
	1000/14.8	142	6.2
	1500/29.8	161	6.4
Mesh	1500/29.8	179	6.6
Wire	1500/29.8	186	7.1

thicker straight jet formations are observed under conditions where the electric field is more uniformly distributed. Furthermore, the envelope angle is influenced by the electric field, with a uniform electric field leading to a narrower whipping motion.

Table 5 summarizes the tensile tests results of as-spun fibers collected via foil, mesh, and wire collectors. Both tensile strength and modulus improve by increasing the collector surface speed. When the surface speed of the collector is increased from 9.9 to 29.8 m/s, the tensile strength increases by 25%. Although Young’s modulus improves with higher collector speed, only minor improvements are observed beyond 14.8 m/s. Both wire and mesh collectors exhibit enhanced stiffness. The nanofibers fabricated with a wire-type collector exhibit the highest tensile strength and Young’s modulus among these collector geometries. By altering the foil-type collector to wire, the tensile strength and modulus improve by 15 and 11%, respectively.

Figure 14a shows the stress-strain curve for nanofiber mats produced using needle, flash, and protruded electrodes. Introducing the protruded electrode elevates the tensile strength of PAN electrospun nanofiber mats from 128 to 148 MPa compared to traditional needle electrodes at 500 rpm. Additionally, there’s a slight increase in Young’s modulus from 5.1 to 5.8 MPa. Although the tensile strength for the flash electrode surpasses that of the needle electrode, both exhibit the same Young’s modulus of 5.1 MPa. Furthermore, **Figure 14b** shows the tensile test results of PAN nanofiber mats fabricated at 1500 rpm by employing a protruded type of electrode. The most enhanced tensile strength is obtained for the nanofibers produced using a wire-type collector, reaching 207 MPa. The improvement in tensile strength is between 10 and 13% when comparing the needle tip to the protruded electrode. However, only moderate enhancement is observed for Young’s modulus. Although the tensile strength improves by 30% by

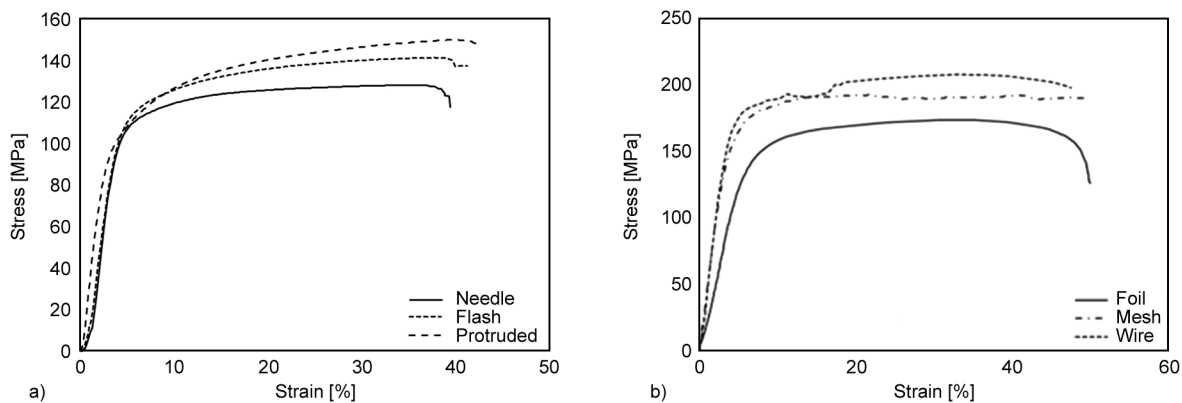


Figure 14. Stress-strain curve of electrospun PAN yarn a) fabricated with needle, flash, and protruded type of electrode where the collector is foil at 500 rpm, b) fabricated with protruded type of collector where the collectors are foil, mesh and wire at 1500 rpm.

altering the collector geometry from foil to wire and using a protrude-type electrode, the enhancement in Young's modulus is only 13%.

The improvement in tensile strength can be explained by fiber morphology, as nanofibers manufactured using the protruded electrode are more uniform and have smaller diameters compared to other electrode types. However, Young's modulus does not improve as much as tensile strength. Less uniform nanofibers may interact with each other more, increasing stiffness.

4. Conclusions

This study investigates the intricate realm of electrospinning nanofibers, specifically focusing on the production of highly aligned PAN nanofibers using an in-house method. The research examines the influence of various collector designs, electrode configurations, and collector speeds on the properties of electrospun nanofibers.

Collector geometry significantly impacts electric field distribution, with wire and mesh collectors providing more intense and uniform fields than foil collectors, resulting in reduced fiber diameters and improved alignment. Collector speed also influences fiber alignment and tensile strength; lower RPMs lead to a wider fiber angle distribution, while wire collectors produce better aligned fibers than mesh and foil collectors. This alignment correlates with mechanical properties, as PAN nanofibers produced at 1500 rpm with wire collectors achieve a tensile strength of about 207 MPa, compared to nanofibers fabricated at 500 rpm with foil collectors, which have a tensile strength of about 128 MPa. SEM and FEA analyses demonstrate that electrode geometry can alter fiber diameter and alignment, reducing the average diameter from 272 to 239 nm and enhancing alignment by nearly 50%.

Overall, this study contributes to the understanding of how variations in collector design, electrode geometry, and collector speed influence the electrospinning process and the properties of the resulting nanofibers. The findings open avenues for further exploration and optimization of electrospinning techniques, with potential applications in various fields, including materials science, biomedical engineering, and energy storage.

Acknowledgements

This research was supported by Turkish Ministry of National Education Ph.D scholarship program YLYS 1416 and The University of Oklahoma School of Aerospace and Mechanical Engineering Department.

References

- [1] Chaos-Morán R., Salazar A., Ureña A.: Mechanical analysis of carbon nanofiber/epoxy resin composites. *Polymer Composites*, **32**, 1640–1651 (2011).
<https://doi.org/10.1002/pc.21187>
- [2] Xia W., Peng G., Hu Y., Dou G.: Desired properties and corresponding improvement measures of electrospun nanofibers for membrane distillation, reinforcement, and self-healing applications. *Polymer Engineering and Science*, **62**, 247–268 (2022).
<https://doi.org/10.1002/pen.25851>
- [3] Shakil U. A., Abu Hassan S. B., Yahya M. Y., Rejab M. R. M.: A focused review of short electrospun nanofiber preparation techniques for composite reinforcement. *Nanotechnology Reviews*, **11**, 1991–2014 (2022).
<https://doi.org/10.1515/ntrev-2022-0116>
- [4] Wang G., Yu D., Kelkar A. D., Zhang L.: Electrospun nanofiber: Emerging reinforcing filler in polymer matrix composite materials. *Progress in Polymer Science*, **75**, 73–107 (2017).
<https://doi.org/10.1016/j.progpolymsci.2017.08.002>
- [5] Zhao X. G., Jin E. M., Park J.-Y., Gu H.-B.: Hybrid polymer electrolyte composite with SiO₂ nanofiber filler for solid-state dye-sensitized solar cells. *Composites Science and Technology*, **103**, 100–105 (2014).
<https://doi.org/10.1016/j.compscitech.2014.08.020>
- [6] Zin M. E., Sutapun W.: Study of parameter affecting morphology of electrospun poly(lactic acid) (PLA) fibers loaded with Ag/CaCO₃ filler. *IOP Conference Series: Materials Science and Engineering*, **1234**, 012009 (2022).
<https://doi.org/10.1088/1757-899x/1234/1/012009>
- [7] Lee J., Lee K. J.: Colloid syringeless electrospinning toward nonwoven nanofiber web containing a massive amount of inorganic fillers. *Macromolecular Materials and Engineering*, **307**, 2100818 (2022).
<https://doi.org/10.1002/mame.202100818>
- [8] Zheng G., Yang Y., Cha J. J., Hong S. S., Cui Y.: Hollow carbon nanofiber-encapsulated sulfur cathodes for high specific capacity rechargeable lithium batteries. *Nano Letters*, **11**, 4462–4467 (2011).
<https://doi.org/10.1021/nl2027684>
- [9] Zhang B., Kang F., Tarascon J.-M., Kim J.-K.: Recent advances in electrospun carbon nanofibers and their application in electrochemical energy storage. *Progress in Materials Science*, **76**, 319–380 (2016).
<https://doi.org/10.1016/j.pmatsci.2015.08.002>

- [10] Gu S. Y., Ren J., Vancso G. J.: Process optimization and empirical modeling for electrospun polyacrylonitrile (PAN) nanofiber precursor of carbon nanofibers. *European Polymer Journal*, **41**, 2559–2568 (2005). <https://doi.org/10.1016/j.eurpolymj.2005.05.008>
- [11] Lee H-M., Kim H-G., An K-H., Kim B-J.: Effects of pore structures on electrochemical behaviors of polyacrylonitrile-based activated carbon nanofibers by carbon dioxide activation. *Carbon letters*, **15**, 71–76 (2014). <https://doi.org/10.5714/CL.2014.15.1.071>
- [12] Yu H., Gao X., Deng Y., Xu S., Chen B., Zhang Y., Zhao H.: Electrospinning preparation and electrochemical properties of Lu₂Ti₂O₇ nanowires, nanotubes and wire-in-tube architectures for their potential lithium-ion battery applications. *Journal of Physics and Chemistry of Solids*, **169**, 110889 (2022). <https://doi.org/10.1016/j.jpcs.2022.110889>
- [13] Wang J., Wang Z., Ni J., Li L.: Electrospinning for flexible sodium-ion batteries. *Energy Storage Materials*, **45**, 704–719 (2022). <https://doi.org/10.1016/j.ensm.2021.12.022>
- [14] Yu H., Deng Y., Chen B., Zhang Y., Zhao H.: Electrospinning preparation and electrochemical properties of BiFeO₃ and GdFeO₃ nanofibers for their potential lithium-ion battery applications. *Journal of Electronic Materials*, **52**, 3008–3017 (2023). <https://doi.org/10.1007/s11664-023-10266-4>
- [15] Di Blasi A., Busacca C., Di Blasia O., Briguglio N., Squadrito G., Antonucci V.: Synthesis of flexible electrodes based on electrospun carbon nanofibers with Mn₃O₄ nanoparticles for vanadium redox flow battery application. *Applied Energy*, **190**, 165–171 (2017). <https://doi.org/10.1016/j.apenergy.2016.12.129>
- [16] Chen A., Liu C., Yu Y., Hu Y., Lv H., Zhang Y., Shen S., Zhang J.: A co-confined carbonization approach to aligned nitrogen-doped mesoporous carbon nanofibers and its application as an adsorbent. *Journal of Hazardous Materials*, **276**, 192–199 (2014). <https://doi.org/10.1016/j.jhazmat.2014.05.045>
- [17] Li C., Yin X., Chen L., Li Q., Wang T.: Porous carbon nanofibers derived from conducting polymer: Synthesis and application in lithium-ion batteries with high-rate capability. *Journal of Physical Chemistry C*, **113**, 13438–13442 (2009). <https://doi.org/10.1021/jp901968v>
- [18] Sun X., Xu J., Zhi X., Zhang J., Hou K., Bian Y., Li X., Wang L., Liang G.: Electrospun organically modified sepiolite/PVDF coating on polypropylene separator to improve electrochemical performance of lithium-ion battery. *Express Polymer Letters*, **18**, 575–591 (2024). <https://doi.org/10.3144/expresspolymlett.2024.43>
- [19] Shao Z., Chen H., Wang Q., Kang G., Wang X., Li W., Liu Y., Zheng G.: High-performance multifunctional electrospun fibrous air filter for personal protection: A review. *Separation and Purification Technology*, **302**, 122175 (2022). <https://doi.org/10.1016/j.seppur.2022.122175>
- [20] Sohrabi M., Razbin M., Pourtavaf M., Bagherzadeh R., Mirmahale M. M.: Exercising hybrid model to design an optimized electrospun polyamide-6 nanofibrous mat for air filtration applications. *Journal of the Textile Institute*, **114**, 1667–1681 (2023). <https://doi.org/10.1080/00405000.2022.2145440>
- [21] Zhou Y., Liu Y., Zhang M., Feng Z., Yu D-G., Wang K.: Electrospun nanofiber membranes for air filtration: A review. *Nanomaterials*, **12**, 1077 (2022). <https://doi.org/10.3390/Nano12071077>
- [22] Luo C., Shao Y., Yu H., Ma H-Z., Zhang Y-H., Gu L., Yin B., Yang M-B.: Preparation and application of high performance PVDF/PS electrospinning film-based triboelectric nanogenerator. *Chemical Physics Letters*, **813**, 140276 (2023). <https://doi.org/10.1016/j.cplett.2022.140276>
- [23] Liao Y., Li Q., Wang N., Shao S.: Development of a new electrochemical sensor for determination of Hg(II) based on bis(indolyl)methane/mesoporous carbon nanofiber/naion/glassy carbon electrode. *Sensors and Actuators B: Chemical*, **215**, 592–597 (2015). <https://doi.org/10.1016/J.SNB.2015.04.006>
- [24] Liu C., Noda Z., Sasaki K., Hayashi K.: Development of a polyaniline nanofiber-based carbon monoxide sensor for hydrogen fuel cell application. *International Journal of Hydrogen Energy*, **37**, 13529–13535 (2012). <https://doi.org/10.1016/j.ijhydene.2012.06.096>
- [25] Wang H., Yang P-H., Cai H-H., Cai J.: Constructions of polyaniline nanofiber-based electrochemical sensor for specific detection of nitrite and sensitive monitoring of ascorbic acid scavenging nitrite. *Synthetic Metals*, **162**, 326–331 (2012). <https://doi.org/10.1016/J.SYNTHMET.2011.12.013>
- [26] Ramya R., Sangaranarayanan M. V.: Electrochemical sensing of glucose using polyaniline nanofiber dendrites-amperometric and impedimetric analysis. *Journal of Applied Polymer Science*, **129**, 735–747 (2013). <https://doi.org/10.1002/App.38770>
- [27] Sharma P. K., Chung J-Y.: Poly-flex-antennas: Application of polymer substrates in flexible antennas. *Express Polymer Letters*, **18**, 371–390 (2024). <https://doi.org/10.3144/expresspolymlett.2024.28>
- [28] Ünsal Ö. F., Bedeloğlu A. Ç.: Nanofiber mat-based highly compact piezoelectric-triboelectric hybrid nanogenerators. *Express Polymer Letters*, **17**, 564–579 (2023). <https://doi.org/10.3144/expresspolymlett.2023.42>
- [29] Xing J., Zhang M., Liu X., Wang C., Xu N., Xing D.: Multi-material electrospinning: From methods to biomedical applications. *Materials Today Bio*, **21**, 100710 (2023). <https://doi.org/10.1016/j.Mtbio.2023.100710>
- [30] Li G., Sun S.: Silk fibroin-based biomaterials for tissue engineering applications. *Molecules*, **27**, 2757 (2022). <https://doi.org/10.3390/Molecules27092757>

- [31] Zhong H., Huang J., Wu J., Du J.: Electrospinning nanofibers to 1D, 2D, and 3D scaffolds and their biomedical applications. *Nano Research*, **15**, 787–804 (2022).
<https://doi.org/10.1007/S12274-021-3593-7>
- [32] Lugoloobi I., Yuanhao W., Marriam I., Hu J., Tebyetekerwa M., Ramakrishna S.: Electrospun biomedical nanofibers and their future as intelligent biomaterials. *Current Opinion in Biomedical Engineering*, **24**, 100418 (2022).
<https://doi.org/10.1016/j.cobme.2022.100418>
- [33] Ramalingam N., Natarajan T. S., Rajiv S.: Preparation and characterization of electrospun curcumin loaded poly(2-hydroxyethyl methacrylate) nanofiber-A biomaterial for multidrug resistant organisms. *Journal of Biomedical Materials Research Part A*, **103**, 16–24 (2015).
<https://doi.org/10.1002/jbm.a.35138>
- [34] Naveen N., Kumar R., Balaji S., Uma T. S., Natrajan T. S., Sehgal P. K.: Synthesis of nonwoven nanofibers by electrospinning – A promising biomaterial for tissue engineering and drug delivery. *Advanced Engineering Materials*, **12**, B380–B387 (2010).
<https://doi.org/10.1002/adem.200980067>
- [35] He B., Yuan X., Jiang D.: Molecular self-assembly guides the fabrication of peptide nanofiber scaffolds for nerve repair. *Royal Society of Chemistry Advances*, **4**, 23610–23621 (2014).
<https://doi.org/10.1039/C4RA01826E>
- [36] Hensley D. K., Melechko A. V., Ericson M. N., Simpson M. L., McKnight T. E.: Transparent microarrays of vertically aligned carbon nanofibers as a multimodal tissue interface. in 'Biomedical Science and Engineering Conference, Biomedical Research and Analysis in Neuroscience, Oak Ridge, USA' 1–4 (2010).
<https://doi.org/10.1109/BSEC.2010.5510801>
- [37] Güler H. K., Çalhoğlu F. C.: A new composite nanofibrous biomaterial development for drug delivery applications. *Express Polymer Letters*, **17**, 487–501 (2023).
<https://doi.org/10.3144/expresspolymlett.2023.36>
- [38] Zou G., Zhang D., Dong C., Li H., Xiong K., Fei L., Qian Y.: Carbon nanofibers: Synthesis, characterization, and electrochemical properties. *Carbon*, **44**, 828–832 (2006).
<https://doi.org/10.1016/j.carbon.2005.10.035>
- [39] Koombhongse S., Liu W., Reneker D. H.: Flat polymer ribbons and other shapes by electrospinning. *Journal of Polymer Science Part B: Polymer Physics*, **39**, 2598–2606 (2001).
<https://doi.org/10.1002/polb.10015>
- [40] Barua B., Saha M. C.: Investigation on jet stability, fiber diameter, and tensile properties of electrospun polyacrylonitrile nanofibrous yarns. *Journal of Applied Polymer Science*, **132**, 41918 (2015).
<https://doi.org/10.1002/App.41918>
- [41] Gañán-Calvo A. M., Rebollo-Muñoz N., Montanero J. M.: The minimum or natural rate of flow and droplet size ejected by Taylor cone-jets: Physical symmetries and scaling laws. *New Journal of Physics*, **15**, 033035 (2013).
<https://doi.org/10.1088/1367-2630/15/3/033035>
- [42] Rosell-Llompart J., Grifoll J., Loscertales I. G.: Electrospays in the cone-jet mode: From Taylor cone formation to spray development. *Journal of Aerosol Science*, **125**, 2–31 (2018).
<https://doi.org/10.1016/j.jaerosci.2018.04.008>
- [43] Tripatanasuwan S., Zhong Z., Reneker D. H.: Effect of evaporation and solidification of the charged jet in electrospinning of poly(ethylene oxide) aqueous solution. *Polymer*, **48**, 5742–5746 (2007).
<https://doi.org/10.1016/j.polymer.2007.07.045>
- [44] Guo Y., Wang X., Shen Y., Dong K., Shen L., Alzabal A. A. A.: Research progress, models and simulation of electrospinning technology: A review. *Journal of Materials Science*, **57**, 58–104 (2022).
<https://doi.org/10.1007/S10853-021-06575-W>
- [45] Zahra F. T., Zhang Y., Ajayi A. O., Quick Q., Mu R.: Optimization of electrospinning parameters for lower molecular weight polymers: A case study on polyvinylpyrrolidone. *Polymers*, **16**, 1217 (2024).
<https://doi.org/10.3390/Polym16091217>
- [46] Ngadiman N. H. A., Noordin M. Y., Idris A., Shakir A. S. A., Kurniawan D.: Influence of polyvinyl alcohol molecular weight on the electrospun nanofiber mechanical properties. *Procedia Manufacturing*, **2**, 568–572 (2015).
<https://doi.org/10.1016/j.promfg.2015.07.098>
- [47] Alharbi N., Daraei A., Lee H., Guthold M.: The effect of molecular weight and fiber diameter on the mechanical properties of single, electrospun PCL nanofibers. *Materials Today Communications*, **35**, 105773 (2023).
<https://doi.org/10.1016/j.Mtcomm.2023.105773>
- [48] Zhou Z., Lai C., Zhang L., Qian Y., Hou H., Reneker D. H., Fong H.: Development of carbon nanofibers from aligned electrospun polyacrylonitrile nanofiber bundles and characterization of their microstructural, electrical, and mechanical properties. *Polymer*, **50**, 2999–3006 (2009).
<https://doi.org/10.1016/j.polymer.2009.04.058>
- [49] Xu C. Y., Inai R., Kotaki M., Ramakrishna S.: Aligned biodegradable nanofibrous structure: A potential scaffold for blood vessel engineering. *Biomaterials*, **25**, 877–886 (2004).
[https://doi.org/10.1016/S0142-9612\(03\)00593-3](https://doi.org/10.1016/S0142-9612(03)00593-3)
- [50] Xie J., MacEwan M. R., Willerth S. M., Li X., Moran D. W., Sakiyama-Elbert S. E., Xia Y.: Conductive core-sheath nanofibers and their potential application in neural tissue engineering. *Advanced Functional Materials*, **19**, 2312–2318 (2009).
<https://doi.org/10.1002/adfm.200801904>
- [51] Xue J., Xie J., Liu W., Xia Y.: Electrospun nanofibers: New concepts, materials, and applications. *Accounts of Chemical Research*, **50**, 1976–1987 (2017).
<https://doi.org/10.1021/Acs.Accounts.7b00218>

- [52] Sun Y., Zhang Y., Guo Y., He D., Xu W., Fang W., Zhang C., Zuo Y., Zhang Z.: Electrical aligned polyurethane nerve guidance conduit modulates macrophage polarization and facilitates immunoregulatory peripheral nerve regeneration. *Journal of Nanobiotechnology*, **22**, 244 (2024).
<https://doi.org/10.1186/S12951-024-02507-3>
- [53] Xue J., Wu T., Xia Y.: Perspective: Aligned arrays of electrospun nanofibers for directing cell migration. *APL Materials*, **6**, 120902 (2018).
<https://doi.org/10.1063/1.5058083>
- [54] Theron A., Zussman E., Yarin A. L.: Electrostatic field-assisted alignment of electrospun nanofibres. *Nanotechnology*, **12**, 384–390 (2001).
<https://doi.org/10.1088/0957-4484/12/3/329>
- [55] Kiselev P., Rosell-Llompart J.: Highly aligned electrospun nanofibers by elimination of the whipping motion. *Journal of Applied Polymer Science*, **125**, 2433–2441 (2012).
<https://doi.org/10.1002/App.36519>
- [56] Haider S., Al-Zeghayer Y., Ahmed Ali F. A., Haider A., Mahmood A., Al-Masry W. A., Imran M., Aijaz M. O.: Highly aligned narrow diameter chitosan electrospun nanofibers. *Journal of Polymer Research*, **B**, 105 (2013).
<https://doi.org/10.1007/S10965-013-0105-9>
- [57] Duan H-W., Jiang J-G., Li B-Y., Li B., He T-H.: Electric field finite element analysis and experimentation of plate-plate type electrospinning machine. *International Journal of Control and Automation*, **7**, 179–190 (2014).
<https://doi.org/10.14257/Ijca.2014.7.7.15>
- [58] Cramariuc B., Cramariuc R., Scarlet R., Manea L. R., Lupu I. G., Cramariuc O.: Fiber diameter in electrospinning process. *Journal of Electrostatics*, **71**, 189–198 (2013).
<https://doi.org/10.1016/j.Elstat.2012.12.018>
- [59] Yang Y., Jia Z., Liu J., Li Q., Hou L., Wang L., Guan Z.: Effect of electric field distribution uniformity on electrospinning. *Journal of Applied Physics*, **103**, 104307 (2008).
<https://doi.org/10.1063/1.2924439>
- [60] Demirtas M. S., Barua B., Saha M. C.: Electrospun carbon nanofibers from polyacrylonitrile solution: Influence of relative humidity on morphology and mechanical properties. in ‘American Society for Composites – 30th Technical Conference, East Lansing, United States’ 1748 (2015).
- [61] Moon S., Farris R. J.: Strong electrospun nanometer-diameter polyacrylonitrile carbon fiber yarns. *Carbon*, **47**, 2829–2839 (2009).
<https://doi.org/10.1016/J.CARBON.2009.06.027>
- [62] de la Mora J. F.: The effect of charge emission from electrified liquid cones. *Journal of Fluid Mechanics*, **243**, 561 (1992).
<https://doi.org/10.1017/S0022112092002829>